Modulation of Nanoparticle Diffusion by Surface Ligand Length and Charge: Analysis with Molecular Dynamics Simulations

Anthony Y. Cui[†] and Qiang Cui[*,‡]

[†]*Weston High School, 444 Wellesley Street, Weston, MA 02493*

[‡]*Departments of Chemistry, Physics and Biomedical Engineering, Boston University, 590 Commonwealth Avenue Boston, MA 02215*

E-mail: qiangcui@bu.edu, Tel:(+1)-617-353-6189

Abstract

To help better interpret experimental measurement of nanoparticle size, it is important to understand how their diffusion depends on the physical and chemical features of surface ligands. In this study, explicit solvent molecular dynamics simulations are used to probe the effect of ligand charge and flexibility on the diffusion of small gold nanoparticles. The results suggest that despite a high bare charge (+18 e), cationic nanoparticles studied here have reduced diffusion constants compared to a hydrophobic gold nanoparticle by merely a modest amount. Increasing the ligand length by 10 CH_2 units also has a limited impact on the diffusion constant. For the three particles studied here, the difference between estimated hydrodynamic radius and radius of gyration is on the order of one solvent layer (3-5 Å), confirming that the significant discrepancies found in the size of similar nanoparticles by recent transmission electron microscopy and dynamic light scattering measurements were due to aggregation under solution conditions. The limited impact of electrostatic friction on the diffusion of highly charged nanoparticles is found to be due to the strong anti-correlation between electrostatic and van der Waals forces between nanoparticle and environment, supporting the generality of recent observation for proteins by Matyushov and co-workers. Including the first shell of solvent molecules as part of the diffusing particle has a minor impact on the total force autocorrelation function but reduces the disparity in relaxation time between the total force and its electrostatic and van der Waals components.

1 Introduction

Nanomaterials are used in many important applications such as imaging,[1–3] catalysis,[4,5] energy[6] and food production.[7,8] To control their stability in solution and interaction with other materials, nanomaterials are often functionalized with surface ligands.[9] For guiding the design of surface functionalization, it is essential to understand how surface ligands impact the physical and chemical properties of nanomaterials. A simple but important physical property is the effective size of the nanomaterial, which can be measured using different techniques, such as transmission electron microscopy (TEM),[10] dynamic light scattering (DLS),[11,12] small angle X-ray scattering (SAXS)[13] and fluctuation correlation spectroscopy (FCS).[14] Due to the different experimental conditions, the measured effective size can vary rather significantly. For example, in a recent study[15] of MTAB ((16-mercaptohexadecyl)trimethylammonium bromide) functionalized gold nanoparticules, the effective radii determined from DLS for a series of particles of different gold cores are approximately three times of the values measured with TEM. Such large differences suggest that the nanoparticles aggregate to a considerable degree in solution; this could occur despite the charged nature of surface ligands because the asymmetric distribution of MTAB ligands[15–19] leaves a considerable degree of exposed hydrophobic areas, which promote aggregation. Taking the larger effective radii of the gold nanoparticules into consideration was important to matching the computed and measured T_2 relaxation times of surface ligands, which were observed to exhibit generally fast dynamics at the sub-nanosecond time scale;[19] whether ligand dynamics are significantly perturbed by aggregation remains to be analyzed systematically.

Another factor that might have contributed, at least in part, to the difference between TEM and DLS measured radii is that the interfacial solvent and counter ions contribute significantly to the hydrodynamic radius (R_H) inferred from the DLS experiment. For proteins in solution,[20] for example, R_H differs from the radius of gyration (R_g) by 20-30% as typical for spherical objects.[21] Since (gold) nanoparticles are often significantly charged,

with the bare surface charge density exceeding 0.1 C/m^2, we expect that interfacial solvent and ion contribute significantly to both equilibrium and dynamic properties of nanoparticles, as observed for ζ potential and electrophoretic mobility in recent studies.[19,22,23] At a qualitative level, we anticipate that charged ligands at the surface slow down diffusion and therefore increase R_H, as discussed for molecular ions[24,25] and recently, for small metal oxide nanoparticles.[26] These previous analyses focused on relatively low values of charge ($< 5e$), thus whether highly charged nanoparticles experience substantially stronger electrostatic friction (thus a larger difference between R_H and R_g) remains to be clarified. Moreover, the difference between R_H and R_g for nanoparticles with flexible surface ligands has not been systematically analyzed. A particular question of interest is whether flexible and charged surface ligands are coupled more strongly with the surrounding solvent and counter ions than rigid ligands, due to the soft modes associated with the collective rearrangements of flexible ligands. Along this line, we note that the behaviors of nanoparticles might differ from colloids,[27] for which length scale separation is better justified.[28]

In this work, we study the diffusion of three small gold nanoparticles with different surface ligands using explicit solvent molecular dynamics simulations, which allow us to explicitly compare R_H and R_g with molecular level of insights. Specifically, we compare three types of surface ligands that differ in length and charge states, and the results help make clear the quantitative contributions of surface charge and ligand flexibility to diffusion and therefore the value of R_H. By analyzing the force-force correlation function of the nanoparticle, we discuss how compensation between electrostatic and van der Waals interactions leads to a rapid decay of the force autocorrelation function[29] and reduced total friction for the cationic particles despite their high apparent charges, as recently recognized for proteins by Matyushov and co-workers;[30] we also explicitly analyze the impact of including the first layer of solvent as part of the diffusing particle, which significantly reduces the relaxation times of electrostatic and van der Waals forces but only slightly modifies the relaxation time of the total force on the particle. These results have implications to the applicability of the

Stokes-Einstein model to nanoparticles with a molecularly rough and charged surface.

In the following, we first summarize the computational models and simulation details. Next, we present the computational results, which include finite size effect on computed diffusion constants, impacts of ligand properties and counter ion concentration on nanoparticle diffusion, and behaviors of velocity and force autocorrelation functions. Finally, we draw a few conclusions.

2 Computational Methods

We study three small gold nanoparticle (Au-NP) systems, which are functionalized with short hydrophobic (-$S(CH_2)_5H$), short cationic (-$S(CH_2)_5NH_3^+$) and long cationic (-$S(CH_2)_{15}NH_3^+$) ligands, respectively; they are referred to $Au_{25}SC5H_{18}$, $Au_{25}SC5N_{18}$ and $Au_{25}SC15N_{18}$, respectively, since they share the same gold core (Au_{25}) and each contains 18 ligands (see Table 1). A very small gold core is chosen in this work so that the molecular nature of the nanoparticle/water interface is prominent (see snapshots in Fig. 1). The structures of the Au-NP systems are set up based on the crystal structures[31,32] of similar gold clusters using the CHARMM-GUI[33] Nanomaterial Modeler. Since the small nanoparticles feature a high surface curvature, all primary amines are assumed to be protonated as they can effectively avoid each other.[34,35]

Table 1: Model ligands used in this work.[a]

Model ligand	Chemical formula
SC5H	-$S(CH_2)_5H$
SC5N	-$S(CH_2)_5NH_3^+$
SC15N	-$S(CH_2)_{15}NH_3^+$

a. Each gold nanoparticle contains 25 Au atoms and is functionalized with 18 ligands; thus the functionalized particles are referred to as $Au_{25}SC5H_{18}$, $Au_{25}SC5N_{18}$ and $Au_{25}SC15N_{18}$. The amine groups are considered to be fully protonated, which is likely a good approximation considering the large curvature of the small Au-NPs studied here.[34,35]

Explicit solvent molecular dynamics simulations are conducted for the nanoparticles in salt solution. Most production runs are conducted with a simulation box of 100 Å in length.

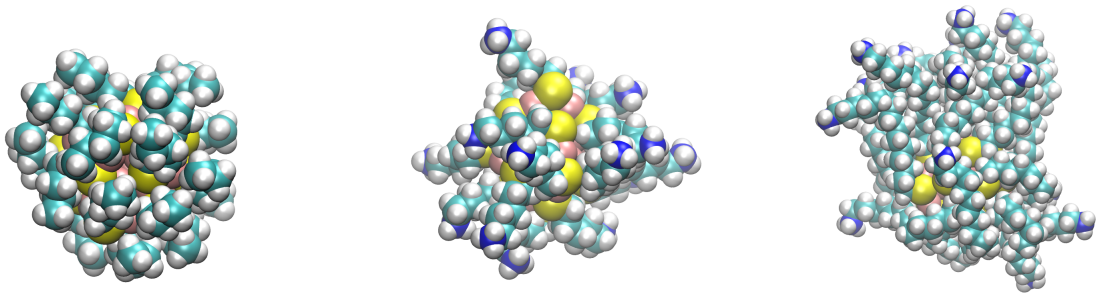

(a) (b) (c)

Figure 1: Snapshots for the Au-NPs studied in this work: $Au_{25}L_{18}$, in which L=SC5H, SC5N and SC15N (see Table 1 for their chemical structures). Among those, $Au_{25}SC5H_{18}$ can be considered to be largely spherical with a uniform surface, while the other two Au-NPs exhibit a significant degree of surface roughness due to the anisotropic packing of charged ligands.

For the cationic particles, simulations >100 ns using smaller boxes are first carried out to more thoroughly sample the ligand configurations; snapshots of the nanoparticles are then solvated in larger boxes for the computation of diffusion constants. For $Au_{25}SC15N_{18}$, we explicitly study the finite size effect on the computed diffusion constant by comparing results with three box sizes (80, 100 and 120 Å). The simulations are conducted with 150 mM NaCl, which is the physiological salt concentration; this choice is motivated by the consideration that gold nanoparticles are extensively used in biological studies.[36–38] For $Au_{25}SC15N_{18}$, a set of simulations with minimal salt (i.e., with only Cl^- ions to neutralize the bare charge of the nanoparticle, which is +18 e) is also conducted for comparison. For a summary of system sizes and lengths of simulations, see Table 2.

The nanoparticles are treated with the INTERFACE force field,[39] which has been shown to describe gold surface and nanoparticles well.[39–41] The salt ions, water molecules and ligands are treated using the standard models available as part of the CHARMM36/CgenFF model;[42–45] since the chemical groups in the ligands are highly similar to those in the protein force field in CHARMM36, the penalty scores are small. The long simulations for examining the solvation structure of nanoparticles and equilibrating ligand configurations have been conducted with OpenMM 7.2[46] using the NPT ensemble, while shorter simulations for the

Table 2: Computational details for simulations conducted in this work.[a]

Au-NP	Box Length (Å)	Number of atoms	Simulation lengths
$Au_{25}SC5H_{18}$	100	∼94,000	8×2 ns
$Au_{25}SC5N_{18}$	55	∼16,800	3×120 ns
$Au_{25}SC5N_{18}$	100	∼94,500	12×2 ns
$Au_{25}SC15N_{18}$	80	∼48,600	120 ns + 12×2 ns
$Au_{25}SC15N_{18}$	100	∼94,510	12×2 ns
$Au_{25}SC15N_{18}$	100[b]	∼94,510	6×2 ns
$Au_{25}SC15N_{18}$	120	∼164,760	12×2 ns
$Au_{25}SC15N_{18}$	100[b,c]	∼94,510	12×2 ns

a. For each charged Au-NP system, a long (∼120 ns) simulation was used with the small box size to collect configurations that were then studied with multiple shorter simulations for the computation of velocity autocorrelation functions. The salt (NaCl) concentration is 150 mM, unless otherwise stated. b. The system density is equilibrated with NPT simulations, which reduces the box size by ∼1-2 Å. c. With minimal salt rather than 150 mM NaCl.

computation of velocity and force autocorrelation functions for the analysis of diffusion and friction, respectively, have been carried out with the CHARMM package[47] interfaced[47,48] with OpenMM 7.2 in the NVE ensemble to minimize the impact of thermostat on the computed correlation functions; the impact of adjusting the solvent density is also explicitly tested and shown to be a few percent on the computed diffusion constant. For the NPT simulations, the Langevin thermostat[49] with a friction constant of 1 ps^{-1} is used for temperature control (T=300 K), and the Monte Carlo barostat is used for pressure control (p=1 bar). For the computation of non-bonded interactions, the Particle-mesh-Ewald method[50] with a grid size ∼ 1 Å is applied to electrostatic interactions. Switching with a switch distance of 10.0 Å and a cutoff of 12.0 Å is applied to the van der Waals interactions. Shake[51] is applied to constrain bonds involving hydrogen atoms, enabling the use of a 2 fs integration time step.

While the diffusion constant can be computed using mean square displacement and the Einstein relation, we use the integration of velocity autocorrelation function since the object of interest is a single nanoparticle; previous studies[52] suggested that it might take a long time for a large Brownian solute to reach its asymptotic behavior, an effect closely related to the long-time tail in the velocity autocorrelation function.[29,53] The apparent diffusion constant

(D_{PBC}) can be computed in the following fashion,[29,54]

$$D_{PBC}(L) = \frac{1}{3}\int_0^\infty C_{vv}(t)dt = \frac{1}{3}\int_0^\infty \langle \mathbf{v}(0)\cdot\mathbf{v}(t)\rangle dt \approx \frac{1}{3}\Big[\int_0^{t^*} \langle \mathbf{v}(0)\cdot\mathbf{v}(t)\rangle dt + \int_{t^*}^\infty a_0' t^{-\frac{3}{2}} dt\Big], \tag{1}$$

in which we explicitly indicate the long-time tail of $C_{vv}(t)$ and the box size (L) dependence of the computed diffusion constant; the choice of t^* and a_0' is discussed below. Finite size corrections due to hydrodynamic considerations have been reported;[55,56] for a cube geometry in 3D, we have

$$D_0 = D_{PBC}(L) + \frac{k_B T\zeta}{6\pi\eta L} \sim D_{PBC}(L) + \frac{2.84 k_B T}{6\pi\eta L}, \tag{2}$$

in which η is the dynamic solvent viscosity. As discussed below, we observe that the correction seems to work well for the present systems and leads to a consistent estimate of D_0 largely independent of the simulation box length L.

3 Results and Discussion

3.1 Surface Ligand Properties

Before discussing nanoparticle diffusion, we first briefly summarize the structural and dynamical features of surface ligands in the three nanoparticle systems. As illustrated by the snapshots in Fig. 1, the particle with short, hydrophobic ligands (-SC5H) features a rather homogeneous surface; by comparison, the short but cationic ligands (-SC5N) feature less homogeneous packing, while the long cationic ligands (-SC15N) feature even more heterogeneous distributions, which lead to a rather rough surface at the molecular scale. These trends are further illustrated by a spherical Voronoi tessellation[57] of the terminal heavy atoms in the ligands (Fig. 2a-c), which indicate a notable degree of ligand clustering in $Au_{25}SC15N_{18}$. Nevertheless, the difference of the maximal and minimal eigenvalues of the moment of inertia tensor averages to about 10%, 11% and 30% of the largest eigenvalue for $Au_{25}SC5H_{18}$, $Au_{25}SC5N_{18}$ and $Au_{25}SC15N_{18}$, respectively, suggesting that the three nanoparticles on av-

erage do not differ significantly from a spherical shape.

As discussed in our recent analysis of similar gold nanoparticles,[19] surface ligands rearrange their conformations at the nanosecond time scale, even for the ligands that exhibit transient clustering or bundling behavior[15–19] due to the long hydrophobic segments. Here we quantify ligand flexibility by the P_2 correlation functions of two vectors for each ligand: the S-N/S-C vector that points from each sulfur to the terminal heavy atom (N or C) in the same ligand, and the terminal C-N/C-C bond vector of each ligand. As shown in Fig. 2d, the correlation in C-N/C-C bond vectors decays much faster, on the order of ∼50 ps for $Au_{25}SC5H_{18}$ and $Au_{25}SC15N_{18}$, and ∼100 ps for $Au_{25}SC5N_{18}$, than the S-N/S-C vectors, which have relaxation times longer than a nanosecond, especially for the case of long cationic ligand. These results are consistent with a picture in which the surface ligands rearrange their overall orientations in nanoseconds, yet locally the terminal groups are able to sample different orientations at a much faster time scale. Importantly, these time scales are substantially longer than the decay time of the particle's velocity autocorrelation function (a few picoseconds, as shown below), thus surface ligand dynamics and particle diffusion are not expected to be tightly coupled.

3.2 Velocity AutoCorrelation (VAC) Function

The VAC functions for the various systems are shown in Fig. 3; the top panels are semi-log plots for normalized VAC functions, while the bottom panels are log-log plots for unnormalized VAC functions, which help clarify the short-time and long-time behaviors, respectively. For a simple Brownian particle of mass m that experiences instantaneous (thus constant) friction ζ, the VAC function is expected to be a single exponential decay[29] with the short time expansion in the following form,

$$C_{vv}(t) = \frac{k_B T}{m} e^{-\frac{\zeta}{m}t} = \frac{k_B T}{m}\Big(1 - \Omega_0^2 \frac{t^2}{2} + \cdots\Big), \tag{3}$$

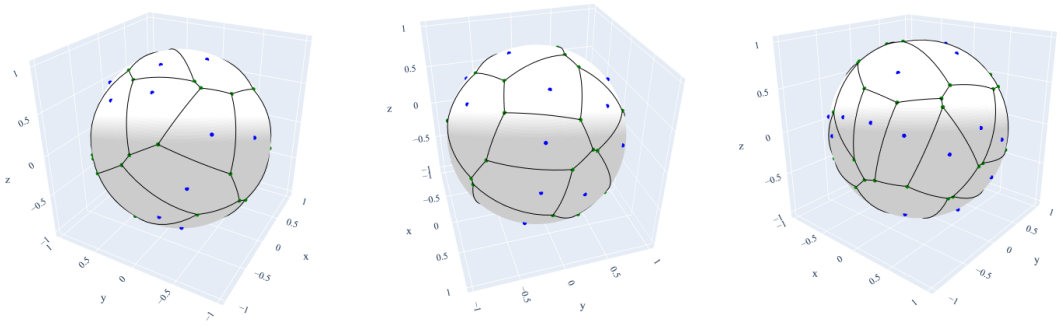

(a) (b) (c)

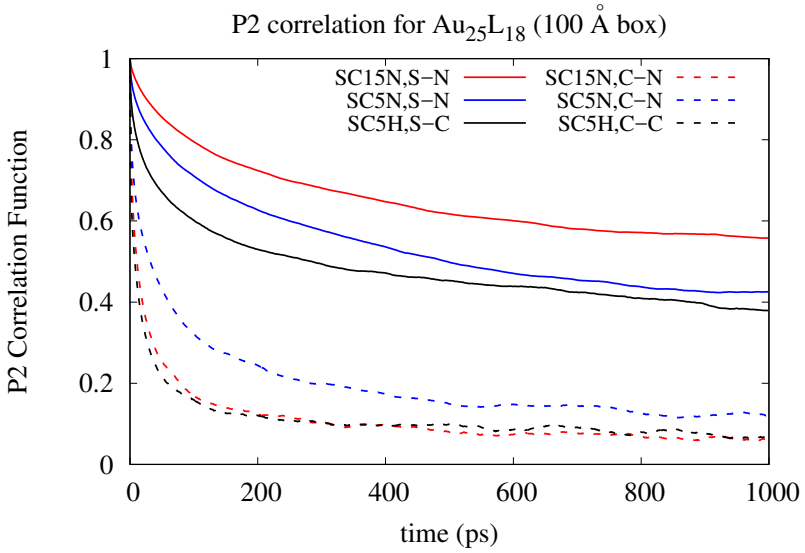

(d)

Figure 2: Structural and dynamical properties of surface ligands. (a-c) Voronoi tessellation[57] of ligand terminal atom projected onto the surface for random snapshots from the Au-NP simulations; the less uniform Voronoi cell areas in (c) is consistent with the more heterogeneous distributions of the long surface ligands in $Au_{25}SC15N_{18}$. (d). P_2 correlation function for two vectors that characterize ligand dynamics; S-N/S-C is the vector from each sulfur to the nitrogen/carbon atom at the end of each ligand; C-N/C-C is the bond vector involving the terminal nitrogen/carbon atom of each ligand.

in which the "Einstein frequency" Ω_0 is given by $\Omega_0^2 = \frac{m}{3k_BT}\langle \dot{\mathbf{v}} \cdot \dot{\mathbf{v}} \rangle = \frac{\langle \delta \mathbf{F}^2 \rangle}{3mk_BT}$; $\mathbf{F}$ is the total force on the particle due to the environment.

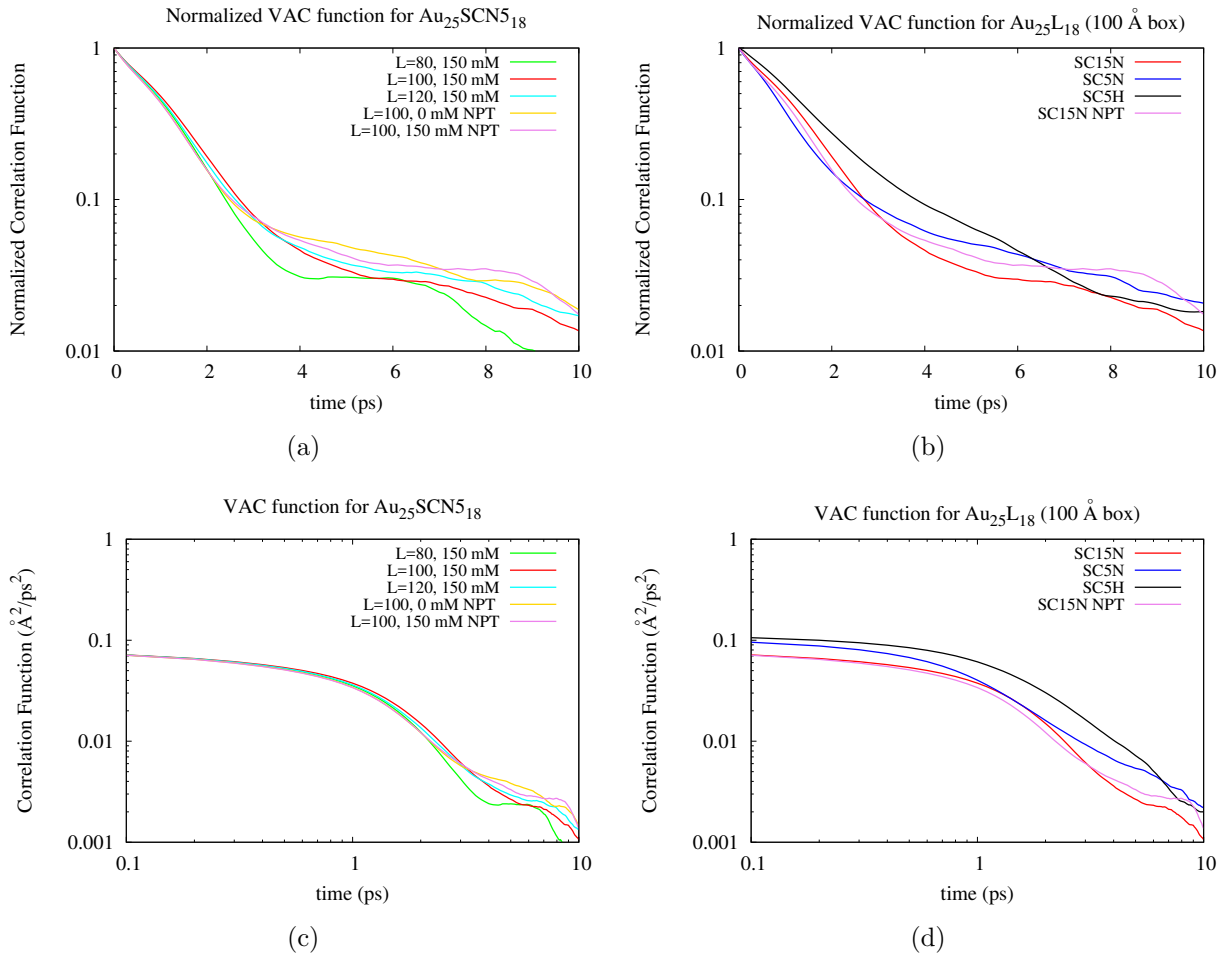

Figure 3: Computed velocity autocorrelation functions for the various nanoparticle systems. (a-b) are semi-log plots for the normalized correlation functions, and (c-d) are log-log plots for the unnormalized correlation functions.

As shown in Fig. 3a-b, the VAC functions are clearly not single exponentials for all the systems studied here, highlighting the complexity of the nanoparticle/environment interactions (see Sect.3.4). We note that even with the shortest ligand, -SC5H, the mass ratio of the nanoparticle and solvent is $\sim 6780/18 \sim 377$, thus the nanoparticle is expected to be well in the Brownian limit.[54] Plotting the unnormalized VAC functions against t (Fig. 4) indicates that Ω_0 is the highest for $Au_{25}SC5N_{18}$ (also see Sect.3.4). This can be explained as the following. For the hydrophobic particle, $Au_{25}SC5H_{18}$, the interaction with the environ-

ment is expected to be weak; a small $\langle \delta \mathbf{F}^2 \rangle$ thus leads to a lower Ω_0. For the two cationic particles, both feature positively charged amines and therefore the magnitude of force fluctuation due to the environment is expected to be similar; however, the particle with the longer ligand is more massive by almost 25% (9595 vs. 7070 amu), leading to a smaller Ω_0 for $Au_{25}SC15N_{18}$. In fact, the initial slopes of the logarithm of VAC functions (expected to be $-\zeta/m$ for a Langevin model) for the two cationic particles have a ratio ∼0.75, which is close to their mass ratio, further supporting that the friction experienced by the cationic particles are similar in magnitude. For additional discussions of friction, see Sect.3.4, which explicitly analyzes the time dependence of particle-environment interactions.

After t reaches the characteristic "hydrodynamic time",

$$t_h = \rho_m R^2/\eta, \tag{4}$$

which is the time taken by a viscous shear wave in the solvent with dynamic viscosity η and mass density ρ_m to propagate across the Brownian particle of radius R, the VAC function is expected reach the asymptotic form that decays algebraically,[29]

$$C_{vv}(t) \sim a_0 t^{-\frac{3}{2}}, \tag{5}$$

in which a theoretical prediction[58] for a_0 is $\frac{2k_BT}{\rho_m(4\pi\eta/\rho_m)^{\frac{3}{2}}} = \frac{2k_BT\sqrt{\rho_m}}{(4\pi\eta)^{\frac{3}{2}}}$, for the limit of heavy particle at infinite dilute concentration and when the particle's diffusion constant is negligible compared to the solvent's kinematic viscosity. For the nanoparticles studied here, the size is in the range of 5-10 Å (see below), the value of t_h is in the range of 0.8 to 3.1 ps; the estimate is made with the viscosity of the TIP3P water model used here,[59] which is lower than the experimental value by almost a factor of 3.[60] Accordingly, the predicted value of a_0 is ∼0.1 $\text{Å}^2 \cdot \text{ps}^{-\frac{1}{2}}$.

Inspection of Fig. 3c-d suggests that the hydrophobic particle $Au_{25}SC5H_{18}$ exhibits behaviors closest to these predictions: the slope of $ln[C_{vv}(t)]$ and $ln[t]$ approaches -1.5 after

t ~2 ps; at t = 2.0 and t = 3.0 ps, the computed $C_{vv}(t)$ values are 0.0300 and 0.0164 $Å^2/ps^2$, respectively; these are in decent agreement with the theoretical predictions ($a_0 t^{-3/2}$) of 0.0361 and 0.0196 $Å^2/ps^2$, respectively. For the cationic particles, the agreement with the theoretical prediction appears to be less good. For $Au_{25}SC5N_{18}$, which has a similar size as $Au_{25}SC5H_{18}$ but charged, the slope of $ln[C_{vv}(t)]$ and $ln[t]$ in the similar time range is slightly shallower than the expected value of -1.5. For $Au_{25}SC15N_{18}$, which is larger in size by at least 3 Å, $ln[C_{vv}(t)]$ vs. $ln[t]$ approximately exhibits the expected slope of -1.5 for t beyond at least 3 ps; the value of $C_{vv}(t)$ is, however, substantially lower than the prediction of $a_0 t^{-3/2}$: at t=5.0 and 6.0 ps, for example, the computed values are 0.0027 and 0.0023 $Å^2/ps^2$, respectively, in comparison to the theoretical predictions of 0.0091 and 0.0069 $Å^2/ps^2$. Finally, it is worth noting that the behavior of $ln[C_{vv}(t)]$ for the small box size of 80 Å is fairly distinct from the larger ones for $t \sim 2-5$ ps (see Fig. 3c), highlighting the finite size effect on VAC function. For more thorough understanding of the long-time tail of $C_{vv}(t)$ for charged particles, more extensive sampling of simulation conditions is likely required.

For the computation of diffusion constant, for the few cases where $C_{vv}(t)$ fits well to the form of $t^{-3/2}$, we fit the prefactor based on $ln[C_{vv}(t)]$ for t in the range of 2.5 and 6.0 ps, and integrate the contribution from the long-time tail analytically starting from t^*=6.0 ps in Eq. 1. As shown in Table 3, the difference between this approach with truncating the integration at 10 ps is a few percent, which is adequate for the current purpose of comparing different systems. Therefore, for the rest cases and discussions, we simply conduct numerical integration of $C_{vv}(t)$ up to t^*=10 ps.

3.3 Diffusion Constant: Finite Size Effect and Impact of Ligand Properties

Using $Au_{25}SC15N_{18}$ as an example, we explicitly examine the finite size effect, as often observed for protein diffusion[55] and other subtle structural features that are sensitive to interfacial water structure and density[61,62]. As shown in Fig. 4a and summarized in Table

3, there is significant finite size effect; with box sizes of 80 and 100 Å, for example, the computed apparent diffusion constants, D_{PBC}, differ by more than 10%. Considering that R_g is only about 8 Å, it is remarkable that with L on the order of 100 Å, the finite size correction derived by Hummer and co-workers[55,56] is almost of the same magnitude as the computed apparent diffusion constant. Encouragingly, once the correction is included, the estimated large-box limit, D_0, is almost identical using simulations with the three box sizes (Table 3). Although the instantaneous shape of the cationic particles is clearly not spherical (see Fig. 1), the ligand rearrangement is fast as discussed in the above subsection, thus the average shape does not deviate significantly from being spherical, explaining the apparent lack of requiring a shape correction factor[63] for the finite size correction.

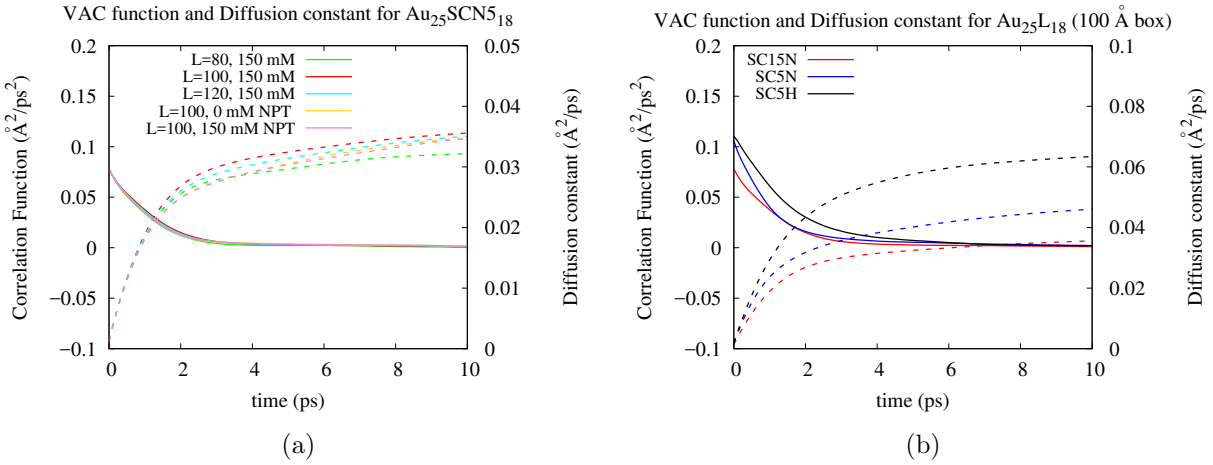

Figure 4: Computed velocity autocorrelation functions (solid lines) and the cumulative time integral, $\frac{1}{3}\int_0^t C_{vv}(\tau)d\tau$ (dotted lines), for the various systems. (a) shows the results for $Au_{25}SC15N_{18}$ under different simulation conditions, and (b) compares results for the three nanoparticles with L=100 Å.

Comparing the diffusion constants for the three nanoparticles, it is evident that both ligand charge and length make notable contributions. While $Au_{25}SC5H_{18}$ and $Au_{25}SC5N_{18}$ have rather similar R_g values of ∼5 Å, the cationic particle has almost 25% reduction in the diffusion constant, highlighting the limited contribution from electrostatic friction (see discussion in Sect.3.4). Increasing the ligand length by ten CH_2 units to $Au_{25}SC15N_{18}$ further decreases the diffusion by another ∼15%. The diffusion constants can be converted to R_H

Table 3: Computed properties for Au-NPs studied in this work.[a]

Au-NP	Box Length (Å)	D_{PBC} (Å^2/ps)	D_0 (Å^2/ps)	R_H (Å)	R_g (Å)
$Au_{25}SC5H_{18}$	100	0.064 (0.062)	0.083	8.2	5.1±0.03
$Au_{25}SC5N_{18}$	100	0.047	0.066	10.4	5.5±0.03
$Au_{25}SC15N_{18}$	80	0.032	0.056	12.2	8.2±0.1
$Au_{25}SC15N_{18}$	100	0.035 (0.034)	0.055	12.4	8.1±0.1
$Au_{25}SC15N_{18}$	100[b]	0.035	0.054	12.6	8.1±0.1
$Au_{25}SC15N_{18}$	120	0.036	0.053	12.8	8.2±0.1
$Au_{25}SC15N_{18}$	100[b,c]	0.036	0.055	12.4	8.2±0.1

a. D_{PBC} is the apparent diffusion constant (Eq. 1); D_0 is the diffusion constant corrected for finite size effect (see Eq. 2); R_H is the hydrodynamic radius estimated using the Stokes-Einstein relation with the stick boundary condition (see Eq. 6); R_g is the radius of gyration. The statistical errors for D_{PBC} are 0.002, 0.003 and 0.004 Å^2/ps for $Au_{25}SC15N_{18}$, $Au_{25}SC5N_{18}$ and $Au_{25}SC5H_{18}$, respectively. The D_{PBC} values without parentheses are obtained by truncating the integration of the velocity autocorrelation function at t=10 ps; values with parentheses are obtained by fitting $C_{vv}(t)$ to the form of $a_0' t^{-3/2}$ in the range of 2-6 ps, and then integrating the contributions from $t > 6$ ps analytically using the fitted a_0' value. b. The system density is equilibrated with NPT simulations, which reduces the box size by ∼1-2 Å. c. With minimal salt rather than 150 mM NaCl.

through the Stokes-Einstein relation with the stick boundary condition (see discussion below for its applicability) as summarized in Table 3. The results indicate that even with long and flexible ligands as -SC15N, the difference between R_H and R_g is limited. The difference of around 4 Å corresponds to one layer of solvent surrounding the cationic groups in the ligand, as supported by the radial distribution function of water oxygen around the ligand nitrogen (Fig. 5a); the strong solvent-nitrogen peak suggests that the residence time for the first layer of solvent is expected to be longer than t_h (Eq. 4) and thus should be considered to be part of the diffusing particle. For the short cationic ligand, -SC5N, the solvent distribution is almost identical (Fig. 5a), thus R_H and R_g differ also by ∼4 Å. For the hydrophobic particle, the solvent doesn't exhibit any significant feature around the ligand (Fig. 5a), thus R_H and R_g differ merely by approximately the excluded solvent size of ∼3 Å, which corresponds to the onset of the solvent-ligand radial distribution function. We note that due to the significant flexibility of surface ligands, water molecules are able to penetrate close to the surface of the nanoparticle, as was illustrated in our previous studies of similar nanoparticles[23,35,64] as well as prior simulation analyses of chromatographic systems.[65]

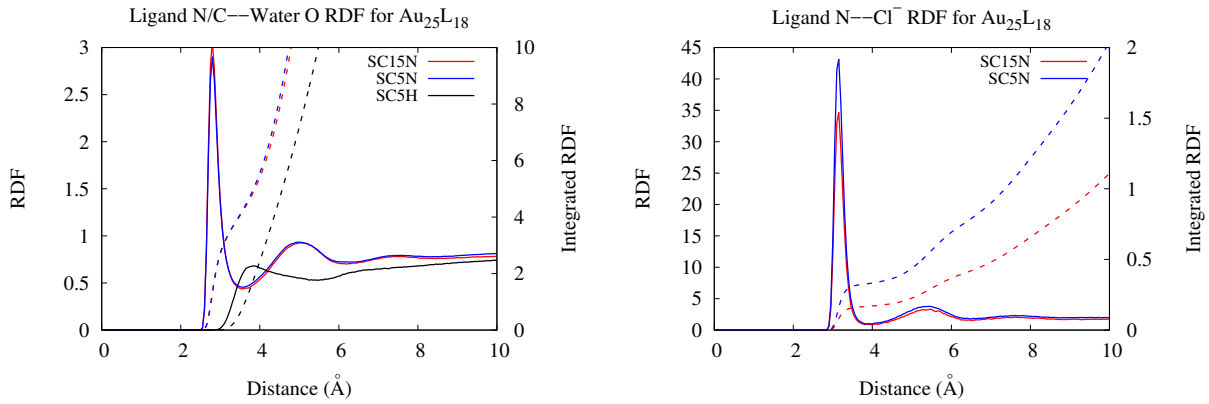

(a) (b)

Figure 5: Radial distribution functions (RDFs) of solvent oxygen (a) and chloride ions (b) around the ligand nitrogen in different nanoparticles from simulations with L=100 Å. The dash lines are the integrated radial distribution functions.

Since both cationic particles bear a considerable degree of charge (+18 e), we also evaluate the contribution of counter ion concentration by running a set of simulations with minimal salt for $Au_{25}SC15N_{18}$. It turns out that the physiological salt concentration only perturbs the diffusion constant by a few percent (Table 3), similar to a previous analysis of metal oxide (phosphotungstate) nanoparticle.[26] The relatively small effect is likely because despite significant enhancement of chloride distribution near the nanoparticle surface, the number of chloride ions tightly associated with the nanoparticle is modest; for $Au_{25}SC15N_{18}$, it is ∼0.15 ion per ligand (Fig. 5b), which corresponds approximately to three chloride ions for the particle; the somewhat low level of association is likely due to the fact that some cationic groups are shielded due to the wrapping of the flexible ligands on the particle surface (see a snapshot in Fig. 1c),[19] which is further supported by the higher level of chloride association observed for the cationic particle with shorter ligands (Fig. 5b). This level of ion association is still possible even under the minimal salt condition, which explains the modest change of diffusion constant.

3.4 Stokes-Einstein Model and Electrostatic friction

The Stokes-Einstein model[66–68] relates the diffusion constant of a spherical Brownian particle with its effective size and solvent viscosity,

$$D_{SE} = \frac{k_B T}{c\pi\eta R_H}, \tag{6}$$

in which c is 4 and 6 for slip and stick boundary conditions, respectively.[69,70] It is derived using a Markovian approximation to the friction kernel (see below), leading to $D_E = \frac{k_B T}{\zeta}$; continuum analysis with different boundary conditions is then used to relate the friction ζ to liquid viscosity η and the (spherical) size of the Brownian particle. As discussed previously,[54,71] for a particle with surface roughness comparable to the solvent size, the solvent can exert torque on the diffusing particle and therefore the stick boundary condition is likely more appropriate. Therefore, for the current study, we use $c = 6$; indeed, if $c = 4$ was used, the R_H will be substantially larger than R_g (e.g., R_H would be 12.3 Å even for the hydrophobic particle, whose R_g=5.1 Å), which is not as physical.

To understand the applicability of the Stokes-Einstein model, it is thus important to examine the behavior of the translational friction, which in general is time dependent and enters the description of diffusion via the generalized Langevin equation (GLE);[29] the time dependence can be written in the form of a memory kernel, $M_\zeta(t)$,

$$\zeta(t) = \zeta(0) M_\zeta(t), \tag{7}$$

in which $\zeta(0) = \frac{\beta}{3}\langle \delta\mathbf{F}^2 \rangle = m\Omega_0^2$. Standard derivations using Fourier-Laplace transform of the generalized Langevin equation lead to the result,[29,30]

$$D_{GLE} = 3[\beta^2 \langle \delta\mathbf{F}^2 \rangle \tau_\zeta]^{-1} = \frac{k_B T}{m\Omega_0^2 \tau_\zeta}, \tag{8}$$

in which $\tau_\zeta = \int_0^\infty M_\zeta(t) dt$ is the relaxation time of the memory function.

It is generally not straightforward to compute $M_\zeta(t)$, which is defined in terms of the auto-correlation function of the *random force* due to the environment.[29,72] It is much more straightforward to compute the auto-correlation function of the *total force* on the particle due to the environment from microscopic simulations (note that the total force includes both frictional and random forces in the GLE framework;[72] in the projection operator framework,[29] the random force is orthogonal to the velocity of the particle),

$$\langle \delta\mathbf{F} \cdot \delta\mathbf{F}(t) \rangle = \langle \delta\mathbf{F}^2 \rangle M_F(t), \tag{9}$$

in which $M_F(t)$ is the normalized total force auto-correlation function with a correlation time τ_F. The normalized VAC function, $C_{vv}(t)/C_{vv}(0)$, $M_\zeta(t)$ and $M_F(t)$ are related to each other with well-establish expressions in terms of their Fourier-Laplace transforms;[29,73] e.g., $[\Omega_0^2 \tilde{M}_\zeta(\omega)]^{-1} = [\Omega_0^2 \tilde{M}_F(\omega)]^{-1} - (i\omega)^{-1}$.

To further understand factors that dictate the diffusion constant, it is thus useful to evaluate τ_F and also various contributions to $\langle \delta\mathbf{F}^2 \rangle$; for example, since $\delta\mathbf{F}$ contains both van der Waals and electrostatic contributions, $\langle \delta\mathbf{F}^2 \rangle$ should contain the corresponding contributions and the cross-correlation of van der Waals and electrostatic terms:

$$\langle \delta\mathbf{F}^2 \rangle = \langle \delta\mathbf{F}_{elec}^2 \rangle + \langle \delta\mathbf{F}_{vdW}^2 \rangle + 2\langle \delta\mathbf{F}_{elec} \cdot \delta\mathbf{F}_{vdW} \rangle \tag{10}$$

Remarkably, in previous work,[25,30] it was observed for proteins that, $\langle \delta\mathbf{F}_{elec} \cdot \delta\mathbf{F}_{vdW} \rangle \approx -\langle \delta\mathbf{F}_{elec}^2 \rangle$, thus,

$$\langle \delta\mathbf{F}^2 \rangle \approx \langle \delta\mathbf{F}_{vdW}^2 \rangle - \langle \delta\mathbf{F}_{elec}^2 \rangle; \tag{11}$$

it is of interest to investigate if this observation applies more broadly to other systems, such as the nanoparticles in the current study.

In Figure 6, we show the normalized force autocorrelation function and its decomposition at both short (< 1 ps) and long (1 ns) time scales for $Au_{25}SC15N_{18}$; the short-time behavior

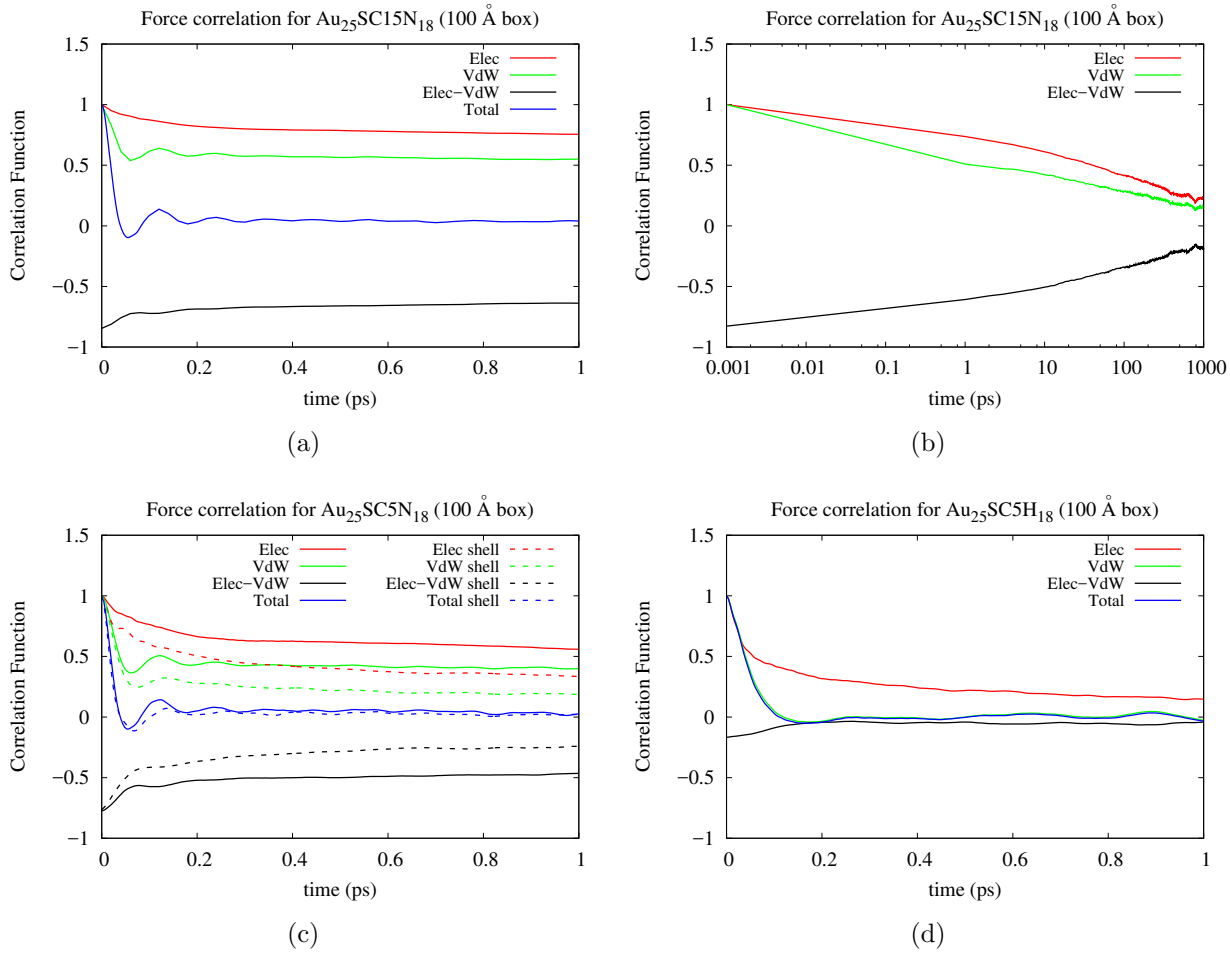

Figure 6: Normalized force autocorrelation functions computed for $Au_{25}L_{18}$ and their electrostatic and van der Waals components as well as the cross correlation between these components. (a) and (b) show the behaviors for $Au_{25}SC15N_{18}$ at different time scales and highlight that the compensation between electrostatic and van der Waals solvent-particle interactions leads to dramatic difference in relaxation time scales for the total force and its components. (c) and (d) show the short time behaviors for $Au_{25}SC5N_{18}$ and $Au_{25}SC5H_{18}$, respectively, which highlight the minimal contribution from electrostatics in the latter case. In (c), the dashed lines are results when the first solvation shell of the ligand nitrogens (see Fig. 5a) is included as part of the diffusing particle.

is also shown for the other two particles for comparison. Similar to previous analysis of protein,[30] for the cationic particles, we also observe that the electrostatic and van der Waals contributions have long correlation times on the nanosecond time scale; moreover, they have strong and persistent anti-correlations, which have an equal (zero) time value of ∼-0.8. As a result, the total force auto-correlation function decays at a much faster time scale of merely ∼ 20 fs (Fig. 6a), which is at least 4-5 orders of magnitude faster than the electrostatic and van der Waals components. The cationic particle with the short ligand exhibits generally similar features, although the electrostatic and van der Waals components relax somewhat faster than $Au_{25}SC15N_{18}$; for example, by ∼ 1 ps, the normalized electrostatic component of $M_F(t)$ decays to ∼0.5 and 0.75 for $Au_{25}SC5N_{18}$ and $Au_{25}SC15N_{18}$, respectively. For the hydrophobic gold particle, the electrostatic component is much weaker and decays on the picosecond time scale (Fig. 6d). The total force correlation is dictated by the van der Waals component, which decays at the timescale of ∼50 fs; i.e., without strong electrostatic interaction, the solvent-particle force correlation in fact decays slower by a factor of two than the cationic particles, again highlighting the significance of compensation between electrostatic and van der Waals components for charged particles.

Table 4: Computed force fluctuations (in the unit of $kcal^2 \cdot mol^{-2} \cdot Å^{-2}$), Einstein frequency ($\Omega_0$, in ps^{-1}), approximate correlation time τ_F (in fs) and GLE diffusion constant (D_{GLE}, in $Å^2/ps$) for Au-NPs studied in this work.[a]

Au-NP	$\langle \delta \mathbf{F}^2_{elec} \rangle$	$\langle \delta \mathbf{F}^2_{vdw} \rangle$	$\langle \delta \mathbf{F}_{elec} \cdot \delta \mathbf{F}_{vdw} \rangle$	$\langle \delta \mathbf{F}^2_{tot} \rangle$	Ω_0 [b]	τ_F [c]	D_{GLE} [d]
$Au_{25}SC5H_{18}$	15	409	-13	399	3.7	39	0.071
$Au_{25}SC5N_{18}$	6060	6890	-4846	3206	10.2	26	0.013
$Au_{25}SC5N_{18}$ [e]	6476	9494	-5969	4030	–	17	0.016
$Au_{25}SC15N_{18}$	9420	9780	-8058	3164	8.8	22	0.016

a. The calculations are based on the 100 Å simulation boxes. b. $\Omega_0^2 = \frac{\langle \delta \mathbf{F}^2_{tot} \rangle}{3mk_BT}$. c. To estimate τ_F, a truncation of 200 fs is introduced to the integration of $M_F(t)$ up to 200 fs (see Fig 6). d. Estimated based on Eq. 8 by approximating τ_ζ by τ_F. e. Calculations that include the solvent/ions within the first solvation shell (3.5 Å) from the ligand nitrogen as part of the diffusing particle.

The compensation between electrostatic and van der Waals forces can also be appreciated by examining the absolute magnitude of the force fluctuations, which are summarized in Table 4). The dominant contribution of the van der Waals component is evident and

expected for the hydrophobic particle, for which $\langle \delta \mathbf{F}^2_{elec} \rangle$ is merely ∼3-4% of $\langle \delta \mathbf{F}^2_{vdw} \rangle$. For the charged particles, strong electrostatic interaction between the particle and the environment also increase $\langle \delta \mathbf{F}^2_{vdw} \rangle$ by a factor of ∼20 relative to the hydrophobic particle; due to the anti-correlation between electrostatic and van der Waals force, however, the total force fluctuations for the cationic particles are about only one order of magnitude higher than the hydrophobic particle. In fact, although the two cationic particles exhibit different values for $\langle \delta \mathbf{F}^2_{elec} \rangle$ and $\langle \delta \mathbf{F}^2_{vdw} \rangle$, they have similar total force fluctuations; for both cases, we note that $\langle \delta \mathbf{F}^2_{tot} \rangle$ is approximately 30-40% of $\langle \delta \mathbf{F}^2_{vdw} \rangle$, which is remarkably similar to previous observation for proteins.[30]

One is tempted to estimate the diffusion constant using Eq. 8 but replacing τ_ζ by τ_F, which is defined as $\int_0^{t_{cut}} M_F(t)dt$, where t_{cut} is an intermediate time between the molecular collision time and relaxation time of the diffusing particle;[73,74] we note that the low-frequency Fourier components of $M_F(t)$ and $M_\zeta(t)$ have distinct trends, and $\tilde{M}_F(0) = \int_0^\infty M_F(t)dt$ in fact approaches 0.[73] Considering their much larger total force fluctuations, the cationic particles are expected to experience stronger frictions and thus expected to have lower diffusion constants than the hydrophobic particle. Indeed, while the strong compensation between electrostatics and van der Waals forces leads to shorter τ_F, using τ_F in Eq. 8 would predict that the D_{GLE} values (see Table 4) for the cationic particles to be ∼5 times lower than the hydrophobic particle, while explicit computations of D_{PBC} in Table 3 show only 30% difference between $Au_{25}SC5N_{18}$ and $Au_{25}SC5H_{18}$. In other words, while D_{GLE} deviates from D_{PBC} by only ∼10% for the hydrophobic particle, the discrepancies are substantially larger for the cationic particles (compare Tables 3 and 4); note that since the key quantities in Eq. 8 are evaluated using the 100 Å box without considering finite size effects, the estimated D_{GLE} should be compared to computed apparent diffusion constant, D_{PBC}, and the difference is about a factor of 2-3. For charged proteins, we note that Matyushov and co-workers[30] also observed that diffusion constant estimated using a simple hydrodynamic (Stokes-Einstein) model did not quantitatively agree with MD results, which found rather weak dependence

of diffusion constant on protein charge (up to $|Q| = 5e$).

One possible origin for the significant discrepancies observed for the cationic particles is that, as discussed in Sect.3.3, the first solvation shell should be considered part of the diffusing cationic particle. To examine this possibility, we re-compute the force fluctuations and autocorrelation functions for $Au_{25}SC5N_{18}$. As shown in Fig. 6c, including the first solvation shell as part of the diffusing particle leads to substantially faster relaxation of both electrostatic and van der Waals forces, as well as their anti-correlation; accordingly, the relaxation time estimated for the total force also becomes somewhat shorter (see Table 4). However, the magnitude of the total force fluctuation, in fact, increases (see Table 4), thus the predicted D_{GLE} value remains substantially different from D_{PBC}.

These observations suggest that for the cationic particles, $M_F(t)$ and $M_\zeta(t)$ are sufficiently different. To match Eq. 8 with the computed D_{PBC} values, the memory function would feature an even shorter relaxation time than the total force autocorrelation function (i.e., $\tau_\zeta < \tau_F$) for the cationic particles. Considering that τ_F is in the range of 20-30 fs, even shorter τ_ζ in the range of 6-10 fs is required; such short relaxation times for the memory function might suggest that a Markovian model (i.e., the Stokes-Einstein model) might be a reasonable approximation, although the VAC functions clearly do not follow the single exponential behavior as expected for a Langevin model (Fig. 3). Therefore, it is worthwhile explicitly investigating the memory function,[29,72] which in principle can be obtained via analysis of the VAC function[75,76] or Fourier transform of the total force auto-correlation function (see above).[29,73] Alternatively, it is also possible that many more independent trajectories with different initial ligand configurations are needed to more accurately compute the short-time behaviors of $M_F(t)$; we note that τ_F was estimated to be about 5-6 fs for azurin in solution,[30] which featured larger force fluctuations ($\langle \delta \mathbf{F}^2 \rangle \sim 10^4$ kcal^2·mol^{-2}·Å^{-2}). More systematic analyses along these lines are left for future work.

4 Conclusions

To help better interpret experimental measurement of nanoparticle size, it is important to understand how their diffusion depends on the physical and chemical features of surface ligands. In this study, using explicit solvent molecular dynamics simulations, we have examined the diffusion behaviors of three gold nanoparticles functionalized with ligands of different charge and flexibility. The results suggest that charge reduces the diffusion constant by a modest amount (25%) despite the significant value of the bare charge (+18 e), while increasing the ligand length by 10 more CH_2 units further reduces diffusion by 15%. Accordingly, the estimated R_H values based on the Stokes-Einstein model do not differ significantly from R_g for the cationic particles. These results help confirm that the discrepancies found in the size of similar nanoparticles by TEM and DLS measurements in Ref. 15 were due to a notable degree of aggregation under solution conditions. The limited impact of electrostatic friction on the diffusion of the nanoparticles is due in large part to the significant anti-correlation between electrostatic and van der Waals interactions between the nanoparticle and environment, as was demonstrated recently for proteins by Matyushov and co-workers,[30] and such strong compensation persists if the first shell of solvent molecules is considered to be part of the diffusing particle. As a result of the compensation, the total force autocorrelation function decays at a much faster time scale (tens of femtoseconds) than the electrostatic and van der Waals components, which relax at the nanosecond time scale; including the first shell of solvent molecules as part of the particle reduces the degree of disparity in the relaxation time scales without significantly affecting the total force autocorrelation function. Nevertheless, using the time scale associated with the total force autocorrelation function as a proxy of the memory function relaxation time underestimates the diffusion constant for charged nanoparticles, while the approximation works fairly well for the hydrophobic nanoparticle. The impact of memory effects of the electrostatic friction on the diffusion of charged nanoparticles deserves to be further analyzed. Along this line, the effect of explicit electronic polarization on the dynamics of highly charged nanoparticles is also of major

interest considering recent discussions of the topic for electrolyte solutions.[77–79]

Acknowledgement

This material is based upon work supported by the National Science Foundation under Grant No. CHE-2001611, the NSF Center for Sustainable Nanotechnology (CSN). The CSN is part of the Centers for Chemical Innovation Program. Computational resources from the Extreme Science and Engineering Discovery Environment (XSEDE), which is supported by NSF grant number OCI-1053575, are greatly appreciated; part of the computational work was performed on the Shared Computing Cluster which is administered by Boston University's Research Computing Services (URL: www.bu.edu/tech/support/research/). QC acknowledges discussions with Professors Arun Yethiraj and Dmitry Matyushov regarding the total force autocorrelation function and the memory function.

References

(1) Chen, G. Y.; Roy, I.; Yang, C. H.; Prasad, P. N. Nanochemistry and Nanomedicine for Nanoparticle-based Diagnostics and Therapy. *Chem. Rev.* **2016**, *116*, 2826–2885.

(2) Li, J. F.; Zhang, Y. J.; Ding, S. Y.; Panneerselvam, R.; Tian, Z. Q. Core-Shell Nanoparticle-Enhanced Raman Spectroscopy. *Chem. Rev.* **2017**, *117*, 5002–5069.

(3) Wegner, K. D.; Hildebrandt, N. Quantum dots: bright and versatile in vitro and in vivo fluorescence imaging biosensors. *Chem. Soc. Rev.* **2015**, *44*, 4792–4834.

(4) Zhao, P. X.; Feng, X. W.; Huang, D. S.; Yang, G. Y.; Astruc, D. Basic concepts and recent advances in nitrophenol reduction by gold- and other transition metal nanoparticles. *Coord. Chem. Rev.* **2015**, *287*, 114–136.

(5) B. Roldan Cuenya,; Behafarid, F. Nanocatalysis: size- and shape-dependent chemisorption and catalytic reactivity. *Surf. Sci. Rep.* **2015**, *70*, 135–187.

(6) Arico, A. S.; Bruce, P.; Scrosati, B.; Tarascon, J.-M.; Van Schalkwijk, W. *Materials For Sustainable Energy: A Collection of Peer-Reviewed Research and Review Articles from Nature Publishing Group*; World Scientific, 2011; pp 148–159.

(7) White, J. C.; Gardea-Torresdey, J. Achieving food security through the very small. *Nat. Nanotech.* **2018**, *13*, 627–629.

(8) Hofmann, T.; Lowry, G. V.; Ghoshal, S.; Tufenkji, N.; Brambilla, D.; Dutcher, J. R.; Gilbertson, L. M.; Giraldo, J. P.; Kinsella, J. M.; M. P. Landry et al., Technology readiness and overcoming barriers to sustainably implement nanotechnology-enabled plant agriculture. *Nat. Food* **2020**, *1*, 416–425.

(9) Zhang, Y. Q.; Tamijani, A. A.; Taylor, M. E.; Zhi, B.; Haynes, C. L.; Mason, S. E.; Hamers, R. J. Molecular surface functionalization of carbon materials via radical-induced grafting of terminal alkenes. *J. Am. Chem. Soc.* **2019**, *141*, 8277–8288.

(10) Yacaman, M. J.; Ascencio, J. A.; Liu, H. B.; Gardea-Torresdey, J. Structure shape and stability of nanometric sized particles. *J. Vacu. Sci. & Tech.* **2001**, *19*, 1091–1103.

(11) Lin, P. C.; Lin, S.; Wang, P. C.; Sridhar, R. Techniques for physicochemical characterization of nanomaterials. *Biotech. Adv.* **2014**, *32*, 711–726.

(12) Bhattacharjee, S. DLS and zeta potential - What they are and what they are not? *J. Control. Release* **2016**, *235*, 337–351.

(13) Li, T.; Senesi, A. J.; Lee, B. Small Angle X-ray Scattering for Nanoparticle Research. *Chem. Rev.* **2016**, *116*, 11128–11180.

(14) Dominguez-Medina, S.; Chen, S.; Blankenburg, J.; Swanglap, P.; Landes, C. F.; Link, S.

Measuring the Hydrodynamic Size of Nanoparticles Using Fluctuation Correlation Spectroscopy. *Annu. Rev. Phys. Chem.* **2016**, *67*, 489–514.

(15) Wu, M.; Vartanian, A. M.; Chong, G.; Pandiakumar, A. K.; Hamers, R. J.; Hernandez, R.; Murphy, C. J. Solution NMR Analysis of Ligand Environment in Quaternary Ammonium-Terminated Self-Assembled Monolayers on Gold Nanoparticles: The Effect of Surface Curvature and Ligand Structure. *J. Am. Chem. Soc.* **2019**, *141*, 4316–4327.

(16) Ghorai, P. K.; Glotzer, S. C. Molecular Dynamics Simulation Study of Self-Assembled Monolayers of Alkanethiol Surfactants on Spherical Gold Nanoparticles. *J. Phys. Chem. C* **2007**, *111*, 15857–15862.

(17) Bolintineanu, D. S.; Lane, J. M. D.; Grest, G. S. Effects of Functional Groups and Ionization on the Structure of Alkanethiol-Coated Gold Nanoparticles. *Langmuir* **2014**, *30*, 11075–11085.

(18) Chew, A. K.; R. C. van Lehn, Effect of Core Morphology on the Structural Asymmetry of Alkanethiol Monolayer-Protected Gold Nanoparticles. *J. Phys. Chem. C* **2018**, *122*, 26288–26297.

(19) Liang, D. Y.; Dahal, U.; Wu, M.; Murphy, C. J.; Cui, Q. Ligand Length and Surface Curvature Modulate Nanoparticle Surface Heterogeneity and Electrostatics. *J. Phys. Chem. C* **2020**, *124*, 24513–24525.

(20) Grimaldo, M.; Roosen-Runge, F.; Zhang, F.; Scheriber, F.; Syedel, T. Dynamics of proteins in solution. *Q. Rev. Biophys.* **2019**, *52*, 1–63.

(21) W. Van De Sande,; Persoons, A. The Size and Shape of Macromolecular Structures: Determination of the Radius, the Length and the Persistence Length of Rodlike Micelles and Dodecyldimenthylammonium Chloride and Bromide. *J. Phys. Chem.* **1985**, *89*, 404–406.

(22) Doane, T. L.; Chuang, C.-H.; Hill, R. J.; Burda, C. Nanoparticle ζ-potentials. *Acc. Chem. Res.* **2011**, *45*, 317–326.

(23) Liang, D. Y.; Dahal, U.; Zhang, Y. Q.; Lochbaum, C.; Hamers, R. J.; Pedersen, J. A.; Cui, Q. Interfacial water and ion distribution determine ζ-potential and binding affinity of nanoparticles to biomolecules. *Nanoscale* **2020**, *12*, 18106–18123.

(24) Bagchi, B. *Molecular Relaxation in Liquids*; Oxford University Press: Oxford, UK, 2012.

(25) Samanta, T.; Matyushov, D. V. Mobility of large ions in water. *J. Chem. Phys.* **2020**, *153*, 044503.

(26) Weiss, L. B.; Dahirel, V.; Marry, V.; Jardat, M. Computation of the Hydrodynamic Radius of Charged Nanoparticles from Nonequilibrium Molecular Dynamics. *J. Phys. Chem. B* **2018**, *122*, 5940–5950.

(27) Nagele, G.; Baur, P. Long-time dynamics of charged colloidal suspensions: hydrodynamic interaction effects. *Physica A* **1997**, *245*, 297–336.

(28) Batista, C. A. S.; Larson, R. G.; Kotov, N. A. Nonadditivity of Nanoparticle Interactions. *Science* **2015**, *350*, 1242477.

(29) Hansen, J.-P.; McDonald, I. R. *Theory of Simple Liquids*; Academic Press: London, 2006.

(30) Sarhangi, S. M.; Matyushov, D. V. Driving Forces of Protein Diffusion. *J. Phys. Chem. Lett.* **2020**, *11*, 10137–10143.

(31) Jadzinsky, P. D.; Calero, G.; Ackerson, C. J.; Bushnell, D. A.; Kornberg, R. D. Structure of a thiol monolayer-protected gold nanoparticle at 1.1 angstrom resolution. *Science* **2007**, *318*, 430–433.

(32) Qian, H. F.; Eckenhoff, W. T.; Zhu, Y.; Pintauer, T.; Jin, R. C. Total Structure Determination of Thiolate-Protected Au-38 Nanoparticles. *J. Am. Chem. Soc.* **2010**, *132*, 8280.

(33) Jo, S.; Kim, T.; Iyer, V. G.; Im, W. CHARMM-GUI: a web-based graphical user interface for CHARMM. *J. Comput. Chem.* **2008**, *29*, 1859–1865.

(34) Wang, D.; Nap, R. J.; Lagzi, I.; Kowalczyk, B.; Han, S.; Grzybowski, B. A.; Szleifer, I. How and Why Nanoparticle's Curvature Regulates the Apparent pKa of the Coating Ligands. *J. Am. Chem. Soc.* **2011**, *133*, 2192–2197, PMID: 21280574.

(35) Hong, J.; Hamers, R. J.; Pedersen, J. A.; Cui, Q. A hybrid molecular dynamics/multiconformer continuum electrostatics (MD/MCCE) approach for the determination of surface charge of nanomaterials. *J. Phys. Chem. C* **2017**, *121*, 3584–3596.

(36) Murphy, C. J.; Vartanian, A. M.; Geiger, F. M.; Hamers, R. J.; Pedersen, J.; Cui, Q.; Haynes, C. L.; Carlson, E. E.; Hernandez, R.; R. D. Klaper et al., Biological Responses to Engineered Nanomaterials: Needs for the Next Decade. *ACS Central Sci.* **2015**, *1*, 117–123.

(37) Jain, S.; Hirst, D.; O'sullivan, J. Gold nanoparticles as novel agents for cancer therapy. *Br. J. Radiol.* **2012**, *85*, 101–113.

(38) Giljohann, D. A.; Seferos, D. S.; Daniel, W. L.; Massich, M. D.; Patel, P. C.; Mirkin, C. A. Gold nanoparticles for biology and medicine. *Angew. Chem. Int. Ed.* **2010**, *49*, 3280–3294.

(39) Heinz, H.; Lin, T.-J.; Kishore Mishra, R.; Emami, F. S. Thermodynamically consistent force fields for the assembly of inorganic, organic, and biological nanostructures: the INTERFACE force field. *Langmuir* **2013**, *29*, 1754–1765.

(40) Liang, D. Y.; Hong, J. W.; Dong, F.; Bennett, J. W.; Mason, S. E.; Hamers, R. J.; Cui, Q. Analysis of Conformational Properties of Amine Ligands at the Gold/Water Interface with QM, MM and QM/MM simulations. *Phys. Chem. Chem. Phys.* **2018**, *20*, 3349–3362.

(41) Geada, I. L.; Ramezani-Dakhel, H.; Jamil, T.; Sulpizi, M.; Heinz, H. Insight into induced charges at metal surfaces and biointerfaces using a polarizable Lennard-Jones potential. *Nat. Comm.* **2018**, *9*, 716.

(42) MacKerell, A. D.; Bashford, D.; Bellott, M.; Dunbrack, R. L.; Evanseck, J. D.; Field, M. J.; Fischer, S.; Gao, J.; Guo, H.; S. Ha et al., All-Atom Empirical Potential for Molecular Modeling and Dynamics Studies of Proteins. *J. Phys. Chem. B* **1998**, *102*, 3586–3616.

(43) Huang, J.; A. D. MacKerell Jr., CHARMM36 All-atom Additive Protein Force Field: Validation Based on Comparison to NMR Data. *J. Comput. Chem.* **2013**, *34*, 2135–2145.

(44) Jorgensen, W. L.; Chandrasekhar, J.; Madura, J. D.; Impey, R. W.; Klein, M. L. Comparison of simple potential functions for simulating liquid water. *The Journal of chemical physics* **1983**, *79*, 926–935.

(45) Vanommeslaeghe, K.; Hatcher, E.; Acharya, C.; Kundu, S.; Zhong, S.; Shim, J.; Darian, E.; Guvench, O.; Lopes, P.; I. Vorobyov et al., CHARMM General Force Field: A Force Field for Drug-Like Molecules Compatible with the CHARMM All-Atom Additive Biological Force Fields. *J. Comput. Chem.* **2010**, *31*, 671–690.

(46) Eastman, P.; Swails, J.; Chodera, J. D.; McGibbon, R. T.; Zhao, Y.; Beauchamp, K. A.; Wang, L. P.; Simmonett, A. C.; Harrigan, M. P.; C. D. Stern et al., OpenMM 7: Rapid Development of High Performance Algorithms for Molecular Dynamics. *PLoS Comput. Biol.* **2017**, *13*, e1005659.

(47) Brooks, B. R.; C. L. Brooks III,; Mackerell, A. D.; Nilsson, L.; Petrella, R. J.; Roux, B.; Won, Y.; Archontis, G.; Bartels, C.; S. Boresch et al., CHARMM: The Biomolecular Simulation Program. *J. Comput. Chem.* **2009**, *30*, 1545–1614.

(48) Lee, J.; Cheng, X.; Swails, J. M.; Yeom, M. S.; Eastman, P. K.; Lemkul, J. A.; Wei, S.; Buckner, J.; J. C. Jeong et al., CHARMM-GUI Input Generator for NAMD, GROMACS, AMBER, OpenMM, and CHARMM/OpenMM Simulations Using the CHARMM36 Additive Force Field. *J. Chem. Theory Comput.* **2016**, *12*, 405–413.

(49) Brünger, A. T. *X-PLOR: version 3.1: a system for x-ray crystallography and NMR*; Yale University Press, 1992.

(50) Darden, T.; York, D.; Pedersen, L. Particle mesh Ewald: An N log (N) method for Ewald sums in large systems. *J. Chem. Phys.* **1993**, *98*, 10089–10092.

(51) Ryckaert, J.-P.; Ciccotti, G.; Berendsen, H. J. Numerical integration of the cartesian equations of motion of a system with constraints: molecular dynamics of n-alkanes. *J. Comput. Phys.* **1977**, *23*, 327–341.

(52) Ould-Kaddour, F.; Levesque, D. Molecular-dynamics investigation of tracer diffusion in a simple liquid: Test of the Stokes-Einstein law. *Phys. Rev. E* **2000**, *63*, 011205.

(53) Alder, B. J.; Wainwright, T. E. Decay of the Velocity Autocorrelation Function. *Phys. Rev. A* **1970**, *1*, 18–21.

(54) Schmidt, J. R.; Skinner, J. L. Hydrodynamic boundary conditions, the Stokes–Einstein law, and long-time tails in the Brownian limit. *J. Chem. Phys.* **2003**, *119*, 8062.

(55) Vögele, M.; Hummer, G. Divergent Diffusion Coefficients in Simulations of Fluids and Lipid Membrane. *J. Phys. Chem. B* **2016**, *120*, 8722–8732.

(56) Linke, M.; Köfinger, J.; Hummer, G. Rotational Diffusion Depends on Box Size in Molecular Dynamics Simulations. *J. Phys. Chem. Lett.* **2018**, *9*, 2874–2878.

(57) Virtanen, P.; Gommers, R.; Oliphant, T. E.; Haberland, M.; Reddy, T.; Cournapeau, D.; Burovski, E.; Peterson, P.; Weckesser, W.; J. Bright et al., SciPy 1.0: fundamental algorithms for scientific computing in Python. *Nat. Methods* **2020**, *17*, 261–272.

(58) Pomeau, Y. Asymptotic Behavior of the Green-Kubo Integrands in Binary Mixtures. *J. Chem. Phys.* **1972**, *57*, 2800–2810.

(59) Mark, P.; Nilsson, L. Structure and Dynamics of the TIP3P, SPC, and SPC/E Water Models at 298 K. *J. Phys. Chem. A* **2001**, *105*, 9954–9960.

(60) Gonzalez, M. A.; Abascal, J. L. F. The shear viscosity of rigid water models. *J. Chem. Phys.* **2010**, *132*, 096101.

(61) El Hage, K.; Hedin, F.; Gupta, P. K.; Meuwly, M.; Karplus, M. Valid molecular dynamics simulations of human hemoglobin require a surprisingly large box size. *eLife* **2018**, *7*, e35560.

(62) Pezzella, M.; El Hage, K.; Niesen, M. J. M.; Shin, S.; Willard, A. P.; Meuwly, M.; Karplus, M. Water Dynamics Around Proteins: T- and R-States of Hemoglobin and Melittin. *J. Phys. Chem. B* **2020**, *124*, 6540–6554.

(63) Yeh, I.-C.; Hummer, G. Diffusion and electrophoretic mobility of single-stranded RNA from molecular dynamics simulations. *Biophys. J* **2004**, *86*, 681–689.

(64) Das, M.; Dahal, U.; Mesele, O.; Liang, D. Y.; Cui, Q. Molecular Dynamics Simulation of Interaction between Functionalized Nanoparticles with Lipid Membranes: Analysis of Coarse-grained Models. *J. Phys. Chem. B* **2019**, *123*, 10547–10561.

(65) El Hage, K.; Gupta, P. K.; Bemish, R.; Meuwly, M. Molecular Mechanisms Underlying Solute Retention at Heterogeneous Interfaces. *J. Phys. Chem. Lett.* **2017**, *8*, 4600–4607.

(66) Einstein, A. *Ann. Physik* **1905**, *17*, 549.

(67) Stokes, G. *Trans. Cambridge Phil. Soc.* **1856**, *9*, 5.

(68) Edward, J. T. Molecular Volumes and the Stokes-Einstein Equation. *J. Chem. Educ.* **1970**, *47*, 261.

(69) Masters, A. J.; Keyes, T.; Madden, P. A. A molecular model of the hydrodynamic stick boundary condition. *J. Chem. Phys.* **1981**, *75*, 485.

(70) Masters, A. J.; Madden, P. A. A molecular theory of Stokes–Einstein behavior. I. Translational Brownian motion. *J. Chem. Phys.* **1981**, *74*, 2450.

(71) Schmidt, J. R.; Skinner, J. L. Brownian Motion of a Rough Sphere and the Stokes-Einstein Law. *J. Phys. Chem. B* **2004**, *108*, 6767–6771.

(72) Zwanzig, R. *Non-equilibrium Statistical Mechanics*; Oxford University Press: Oxford, UK, 2001.

(73) Kubo, R.; Toda, M.; Hashitsume, N. *Statistical Physics II: Nonequilibrium Statistical Mechanics*; Springer: New York, 2003.

(74) Kirkwood, J. G. The Statistical Mechanical Theory of Transport Processes I. General Theory. *J. Chem. Phys.* **1946**, *14*, 180–201.

(75) Harp, G. D.; Berne, B. J. Time-Correlation Functions, Memory Functions and Molecular Dynamics. *Phys. Rev. A* **1970**, *2*, 975–996.

(76) Berkowitz, M.; Morgan, J. D.; Kouri, D. J.; J. A. McCammon, Memory kernels from molecular dynamics. *J. Chem. Phys.* **1981**, *75*, 2462–2463.

(77) J. G. McDaniel,; Yethiraj, A. Influence of Electronic Polarization on the Structure of Ionic Liquids. *J. Phys. Chem. Lett.* **2018**, *9*, 4765–4770.

(78) Panagiotopoulos, A. Z. Simulations of activities, solubilities, transport properties, and nucleation rates for aqueous electrolyte solutions. *J. Chem. Phys.* **2020**, *153*, 010903.

(79) Bedrov, D.; Piquemal, J.-P.; Borodin, O.; A. D. MacKerell Jr.,; Roux, B.; Schröder, C. Molecular Dynamics Simulations of Ionic Liquids and Electrolytes Using Polarizable Force Fields. *Chem. Rev.* **2019**, *119*, 7940–7995.

Graphical TOC Entry